Ionization state and dielectric constant in cold rarefied hydrocarbon plasmas of inertial confinement fusion

A. Shvydky,* A. V. Maximov, V. V. Karasiev, D. Haberberger, S. X. Hu, and V. N. Goncharov
Laboratory for Laser Energetics, University of Rochester, Rochester, New York 14623, USA

(Received 15 January 2021; accepted 2 September 2021; published 21 October 2021)

A combined approach to study cold rarefied matter is introduced that includes a semianalytical method based on the free-energy minimization and *ab initio* calculations based on the finite-temperature density-functional theory. The approach is used to calculate the ionization state of hydrocarbon (CH) under the shock-release conditions in inertial confinement fusion. The dielectric constant of CH is calculated using the Kubo-Greenwood formulation and contribution from atomic polarizabilities is found to be as important as the free-electron contribution. Using the ionization state and dielectric constant, the electron density profile in the rarefaction wave of the shock-release plasma is obtained.

DOI: 10.1103/PhysRevE.104.045207

I. INTRODUCTION

Inertial confinement fusion (ICF) has been an active field of research for more than 50 years [1–4] because of its application as a future energy source. In laser-driven ICF, a cryogenically cooled thin spherical shell of deuterium-tritium (DT) fuel is imploded and compressed by material ablation to form a high-density confinement around a central core where conditions for thermonuclear ignition can be created. During the implosion, the ablation pressure launches multiple shocks through the DT shell and accelerates it inward. Later, the buildup of the pressure in the compressing vapor region decelerates the shell, and at stagnation, creates the conditions in the central core closest to ignition. The pressure buildup and the temperature and density in the core at stagnation are strongly affected by the amount of material that is released from the shell into the vapor region during the implosion.

It is very challenging to measure the material release from the shell in the imploding capsule. However, in a planar geometry, one can access similar conditions with a CH foil and probe it using optical interferometry [5]. It was used for the first time in recent experiments [6] to diagnose the low-density part of the rarefaction wave formed when the shock driven by two OMEGA EP [7] laser beams breaks out of a hydrocarbon (CH) foil. The optical interferometry produces images in the focal plane that are determined by the optical path (phase) that is accumulated by the wavefront of the probe laser propagating through the region of interest. The images are analyzed to obtain spatial profiles of the index of refraction. In low-density and low-temperature conditions, such as in the shock-release material, the plasma is partially ionized and the index of refraction is expected to have contribution from bound electrons in atoms and contribution from free electrons. Densities of atoms and free electrons are connected by the ionization state Z. Therefore, the index of refraction and Z are required to deduce the density profiles from the interferograms.

The index of refraction at low densities and temperatures of shock release material at a specific wavelength of the laser probe ($\lambda_0 = 263$ nm for OMEGA EP interferometry laser) is not generally expected to be available. While there are many studies of optical properties of the CH at the solid or a few times the solid density (see, e.g., Refs. [8–13]), no experimental data are available for the rarefied CH gas at (10^{-4} to 10^{-2}) g/cm^3 and few electronvolt temperatures. Recently *ab initio* simulations became popular and accessible for calculating optical properties of arbitrary materials (see, e.g., Refs. [14,15]) and can be used to obtain the index of refraction at a desired laser frequency and thermodynamic conditions, i.e., mass density ρ and temperature T. The ionization state Z for CH material as a function of ρ and T is traditionally available via numerous Z tables [16–20] used in ICF radiation-hydrodynamics codes [21–24]. The simulations and analysis of the shock-release experiments [6] used the Astrophysical Opacity Tables (AOT) [16] and Collisional Radiative Equilibrium (CRE) tables [17], which predict somewhat different Z for the release conditions, and used the plasma index of refraction, which does not have the atomic contribution. These shortcomings motivated the present investigation.

In this article we calculate the ionization state Z and the dielectric constant (which we use to obtain the index of refraction) as a function of density and temperature under conditions relevant to shock release. The conditions span (10^{-4}to10^{-2}) g/cm^3 in density at a few electronvolts in temperature. We develop an algorithmically transparent, easy-to-follow method, referred to as the Saha-Fermi-Debye-Hückel (SFDH) method, for calculating Z which is based on the free-energy minimization approach [25,26], with free energy containing nonideal terms accounting for binary collisions [27,28] and Coulomb interactions [26,29]. We also obtain Z using *ab initio* calculations based on the Mermin-Kohn-Sham density-functional theory (DFT) [30–33] and test it against the semianalytical SFDH method. After verifying

*ashv@lle.rochester.edu

TABLE I. Approaches used to obtain the ionization state Z, atomic polarizability α of H and C, and dielectric constant ϵ. ϵ_p is the plasma dielectric constant.

Z	α	ϵ
SFDH	α_H (analytical)	DFT (SCAN)
DFT (PBE)	α_C Refs. [35,36]	ϵ_p
AOT	DFT (SCAN)	
CRE		

the DFT-calculated Z, we use the electron population states obtained with the DFT and Kubo-Greenwood formulation [34] to calculate the dielectric constant. Using the combined approach outlined above we found that (a) Z calculated with SFDH method is in good agreement with Z from DFT calculations and both are within 0.2 of either CRE table or AOT table Z's, (b) DFT-calculated atomic polarizabilities are estimated to be within 20% of the reference data, and (c) a fit to the DFT-calculated dielectric constant contains an extra term due to atomic polarizabilities (i.e., contributions from bound states of electrons in atoms) that dominates the dielectric constant at low temperatures. For convenience, Table I contains physical quantities that were compared in the paper and approaches that were used to obtain these quantities. Based on these calculations, we revisited the shock-release experiments [6] and found more accurate electron density profiles, which, however, have not changed the main conclusions of that paper.

This article is organized as follows: In Sec. II we present semianalytical SFDH method for calculating the ionization state Z. In Sec. III we compare Z calculated using the developed method with the DFT calculations and with AOT and CRE tables. In Sec. IV we calculate atomic polarizabilities of H and C atoms. In Sec. V we present DFT calculations of the dielectric constant of CH. In Sec. VI, we use DFT-calculated dielectric constant to revisit the shock release experiments [6]. In Sec. VII, conclusions are drawn.

II. FREE-ENERGY MINIMIZATION METHOD

The free energy of a gas consisting of C and H ions of different ionization states and electrons is written as

$$F = F_0 + F_b + F_c, \tag{1}$$

where

$$F_0 = -kT \sum_{mij} N_{mij} \ln \left[\frac{eV}{N_{mij}} \left(\frac{m_m kT}{2\pi\hbar^2} \right)^{3/2} g_{mij} \right] + \sum_{mij} N_{mij} E_{mij} - kT N_e \ln \left[\frac{eV}{N_e} \left(\frac{m_e kT}{2\pi\hbar^2} \right)^{3/2} \right] \tag{2}$$

is the free energy of the nondegenerate ideal gas [37] of a multispecies system that includes free electrons and ions (neutrals are considered zero charge ions) of different species (chemical elements) and F_b and F_c are nonideal terms described below. Since we are interested in temperatures above 1 eV (11 605 K), we expect the CH material to be fully atomized, so only atoms of C and H in various excitation and ionization states and free electrons are included in Eq. (2). The summation index m denotes species (H or C), index i denotes ion types ($i = 0$ denotes neutrals and $i > 0$ denotes i-times ionized ions), and j denotes bound states of each ion type of each species ($j = 0$ is the ground state and $j > 0$ are the excited states). For a bound state j of ion type i of species m, N_{mij} is the particle number, g_{mij} is the degeneracy, and E_{mij} is the energy defined as

$$E_{mij} = E^*_{mij} + \sum_{i'<i} I_{mi'}, \tag{3}$$

where E^*_{mij} is the excitation energy of bound state j of ion type i and $I_{mi'}$ is the ionization energy of ion type i' of species m. In other words, E_{mij} is the total energy required to bring a neutral atom, $i = 0$, of species m from the ground state, $j = 0$, to the i-times ionized ion in the excited state j. In Eq. (2), N_e is the number of free electrons, m_m is the mass of species m, m_e is the electron mass, k is the Boltzmann constant, $\hbar$ is the reduced Planck constant, V is the volume, T is the temperature, and e is the base of natural logarithm, $e = 2.71828$. For convenience, Table II shows ion types and numbers of excitation energy levels (taken from Ref. [38]) included in the sum over mij in Eq. (2).

To account for short-range, binary interactions between particles, we add the Fermi's hard-sphere excluded-volume term [27,28] to the free energy

$$F_b = -kT \sum_s N_s \ln \left(1 - \frac{b}{V} \right) \approx kT \frac{b}{V} N_{\text{tot}}, \tag{4}$$

where s is a compound index that runs over all bound states of all ions of all species plus free electrons, N_{tot} is the number of all particles,

$$N_{\text{tot}} = \sum_{mij} N_{mij} + N_e = \sum_s N_s, \tag{5}$$

and

$$b = \frac{4\pi}{3} \frac{1}{2N_{\text{tot}}} \sum_{s,t} N_s N_t (r_s + r_t)^3, \tag{6}$$

where the double sum is over compound indexes s and t and then r_s and r_t are effective radii of particles s and t, respectively. The radius r_s of ion type i in bound state j with excitation energy E^* is taken to be equal to the radius of the electron orbit in a classical hydrogen-like atom with charge i and energy E^* (see Appendix), which is a good approximation for highly excited states which constitute the large majority of all bound states. The radii of free electrons and fully ionized ions (i.e., particles with no bound states) in Eq. (6) are zero within the described method. The contribution to the free energy due to binary interactions between particles [Eq. (4)] is characterized by quantity b [Eq. (6)] which is an effective total

TABLE II. Ion types and corresponding numbers of energy states included in Eq. (2). H II (C VII) denotes a fully ionized hydrogen (carbon) ion.

H I	H II	C I	C II	C III	C IV	C V	C VI	C VII
40	1	401	85	133	90	100	81	1

interaction volume. The expansion on the right-hand side of Eq. (4) is valid when $b/V \ll 1$. The last term in Eq. (1) is the contribution to the free energy from the Coulomb interaction between charged particles given by Debye-Hückel formula [26,29]:

$$F_c = -\frac{1}{12\pi}\left(\frac{e_0}{\sqrt{\epsilon_0}}\right)^3 \frac{1}{\sqrt{kTV}}\left(\sum_s Z_s^2 N_s\right)^{3/2}, \tag{7}$$

where e_0 is elementary charge, ϵ_0 is vacuum dielectric permittivity, and Z_s is the charge number of ions i ($Z_{mij} = Z_{mi} = i$) and free electrons ($Z_e = -1$).

By minimizing the free energy from Eq. (1) with respect to the number of particles, following stoichiometric relations for excitation and ionization processes (see Refs. [25,26]), one can obtain a system of equations for the particle numbers of each bound state of each ion type of each species and for the number of free electrons. For bound states of ion type i of species m, the equations that determine the minimum of the free energy are [27]

$$\frac{\partial F}{\partial N_{mij}} - \frac{\partial F}{\partial N_{mij'}} = 0, \tag{8}$$

which includes all combinations of bound states j and j' of ion type i of species m. Substituting free energy from Eq. (1) into Eq. (8) one obtains the following system of equations for the numbers of particles in bound states [27]:

$$N_{mij} = \frac{N_{mi}}{u_{mi}} g_{mij} \exp\left(-\frac{E_{mij}}{kT}\right) \times \exp\left[-\frac{4\pi}{3V}\sum_s N_s (r_s + r_{mij})^3\right], \tag{9}$$

where

$$N_{mi} = \sum_j N_{mij} \tag{10}$$

is the total number of ions of species m in ion state i and

$$u_{mi} = \sum_j g_{mij} \exp\left(-\frac{E_{mij}}{kT}\right) \times \exp\left[-\frac{4\pi}{3V}\sum_s N_s (r_s + r_{mij})^3\right] \tag{11}$$

is the partition function of bound states of ion type i of species m. The second exponential term in Eq. (11) is the consequence of addition of F_b [Eq. (4)] to the free energy [Eq. (1)]. This term reduces contribution of higher excited states to the partition function because of the increase of their radii r_s as $\sim n^2$, where n is the main quantum number. This approach consistently introduces a cutoff to the otherwise divergent sum (see a detailed discussion in [25]). Term F_c in the free energy does not contribute to Eq. (8).

The system of equations for the equilibrium condition of the ionization process has the following form [37]

$$\frac{\partial F}{\partial N_{mij}} - \frac{\partial F}{\partial N_{m(i+1)j'}} - \frac{\partial F}{\partial N_e} = 0, \tag{12}$$

which includes all combinations of j and j', where j is a bound state of ion type i of species m and j' is a bound state of ion type $(i+1)$ of the same species m. Substituting Eq. (1) into Eq. (12) and using Eq. (9), one obtains a system of modified Saha equations for the total number of ion types i of species m, N_{mi}, and the number of free electrons N_e:

$$\frac{N_e N_{m(i+1)}}{N_{mi}} = \frac{u_{m(i+1)}}{u_{mi}}\left[V\left(\frac{m_e kT}{2\pi\hbar^2}\right)^{3/2}\right] \times \exp\left(-\frac{4\pi}{3V}\sum_s N_s r_s^3\right) \exp\left[\frac{\Delta I_{m(i+1)}}{kT}\right], \tag{13}$$

where

$$\Delta I_{m(i+1)} = \frac{Z_{m(i+1)}}{4\pi}\left(\frac{e_0}{\sqrt{\epsilon_0}}\right)^3 \frac{1}{\sqrt{kTV}}\left(\sum_s Z_s^2 N_s\right)^{1/2}.$$

Equations (9), (10), and (13) together with equations representing conservation of the total number of ions (number of nuclei) of each species N_m,

$$\sum_i N_{mi} = N_m, \tag{14}$$

and conservation of charge,

$$\sum_{mi} Z_{mi} N_{mi} = N_e, \tag{15}$$

form a system of nonlinear equations with respect to N_{mij} and N_e. It is solved (see Appendix) to obtain the average ionization state

$$Z = \frac{N_e}{N}, \tag{16}$$

where

$$N = \sum_m N_m \tag{17}$$

is the total number of ions. The presented method of calculating the average ionization state is used to calculate Z for different values of ρ and T and to obtain the function $Z(\rho, T)$.

To summarize, the SFDH method uses the free-energy minimization approach to derive modified Saha equations. Nonideal contributions to the free energy are approximated with the Fermi's excluded-volume term to account for short-range binary interactions and with the Debye-Hückel term to

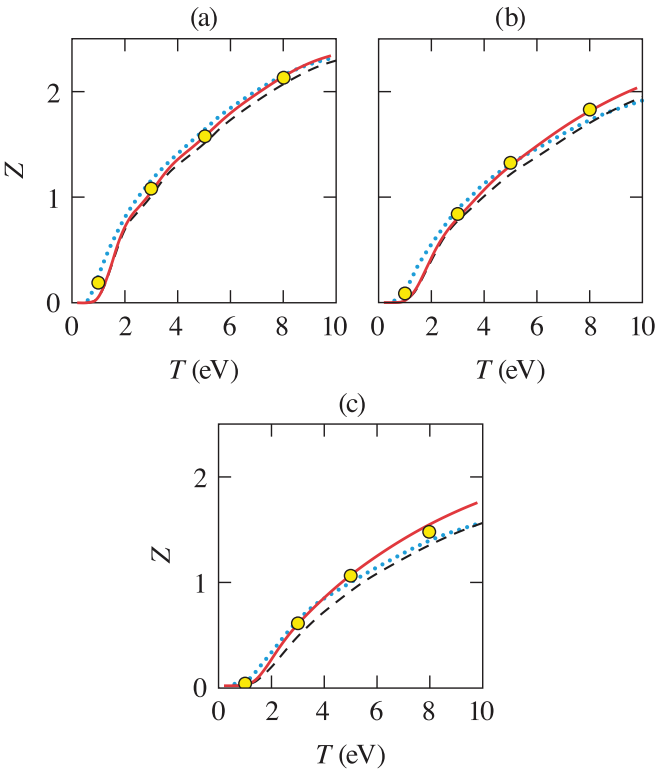

FIG. 1. Average ionization state Z as a function of temperature from four different models: AOT (black dashed lines), CRE (blue dotted lines), our SFDH method (red solid lines), and the DFT calculations (yellow circles) for three mass densities (a) 10^{-4} g/cm^3, (b) 10^{-3} g/cm^3, and (c) 10^{-2} g/cm^3.

account for long-range Coulomb interactions. The approximations are expected to work well in low-density classical plasmas when the Fermi's excluded volume is much smaller than the total volume and the energy of Coulomb interactions between neighboring particles is much smaller than the particle thermal energy. The originality and strength of our approach is that the system of about a thousand of equations (determined by the number of included excited states of all species) [Eqs. (9), (10), (13), (14), and (15)] is solved numerically using a robust algorithm described in the Appendix. The method does not use the low-excitation approximation (see Ref. [25]) and does not linearize the interaction between excited states.

III. IONIZATION STATE

In this section we calculate the ionization state of CH for conditions in the rarefaction wave of shock release experiment [6], which correspond to partially ionized low-density 50 %C-50 %H gas of (1 to 8) eV temperature, ionization state $Z \sim 1$, and (10^{-4} to 10^{-2}) g/cm^3 mass density (very low compared to the solid density of CH of $\sim$1.0 g/cm^3).

Figure 1 shows the average ionization state Z as a function of temperature T for three mass densities ρ. The ionization state in Fig. 1 was obtained using four different sources: AOT [16] tables, CRE tables [17], results of our SFDH method, and *ab initio* calculations.

The *ab initio* calculations of Z used the Mermin-Kohn-Sham DFT [30–33] and were performed using the Vienna Ab initio Simulation Package [33] with the Perdew-Burke-Ernzerhof (PBE) exchange-correlation (XC) functional [39]. The electron-ion electrostatic interaction was modeled with the standard projector augmented wave data set with the plane-wave energy cutoff of 800 eV. The real-space cell size was large enough (12.93 Å or larger) to employ the Baldereschi's mean value point sampling of the Brillouin zone [40]. We also used more accurate although more computationally expensive strongly constrained and appropriately normed (SCAN) metageneralized gradient approximation (meta-GGA) XC functional [41] implemented in the KGEC@QUANTUM-ESPRESSO [15,42] package. Values of Z calculated with SCAN XC functional were virtually identical to those obtained with the PBE XC functional, so the latter was used to obtain Z in this section.

The DFT method calculates the electron states and their occupation numbers for each thermodynamic condition allowing to predict the number of free electrons in the continuum. At finite temperatures the density of electron states consists of a discrete part corresponding to bound states followed by a densely distributed quasicontinuous part corresponding to free-electron (continuum) states. The energy of the continuum edge, E_c, can be readily identified from calculated density of states data (see, e.g., Fig. 7 in Ref. [43] and Figs. 4(b) and 4(d) in Ref. [44]). The number of free electrons is found by summing up the occupation numbers of states with energies above E_c, and Z is found by dividing the number of free electrons by the number of ions in the simulation box.

First we performed molecular dynamics (MD) simulations with eight atoms (four carbon atoms and four hydrogen atoms) in cubic supercell for the highest material density ($\rho = 10^{-2}$ g/cm^3) at the lowest temperature $T = 1$ eV and found that for such a low density the Z value has negligible dependence on the MD snapshots (ionic configurations along the MD trajectory). Then we calculated Z using a simplified scheme with two atoms placed in the fixed body-centered cubic (bcc) cell positions and found very small difference (less than 1%) as compared to the MD snapshot calculations. This approach is a variation of the *single-atom-in-a-cell* method introduced in Ref. [44] and successfully applied to calculation of optical properties in dense silicon plasmas. The difference for lower than $\rho = 10^{-2}$ g/cm^3 densities and higher than $T = 1$ eV temperatures is expected to be even smaller. Therefore we performed such simplified two-atom calculations for the rest of thermodynamic conditions. The number of thermally occupied bands included in the calculation grows very fast as the density decreases and/or the temperature increases. The number of bands was varied between 512 (at $\rho = 10^{-2}$ g/cm^3, $T = 1$ eV) and 64 000 (at $\rho = 10^{-4}$ g/cm^3, $T = 8$ eV) making these calculations extremely computationally expensive at densities below 10^{-3} g/cm^3 and T above 5 eV.

Figure 1 shows that DFT calculations (yellow circles) are in a very good agreement with calculations using SFDH method (red solid lines) at 3-, 5-, and 8-eV temperatures. The larger difference of $\sim$0.07 in Z between the DFT and SFDH at $T = 8$ eV and $\rho = 10^{-2}$ g/cm^3 (see Fig. 1) can be explained by XC thermal effects which are not taken into account by the ground state SCAN and PBE density functionals. The XC

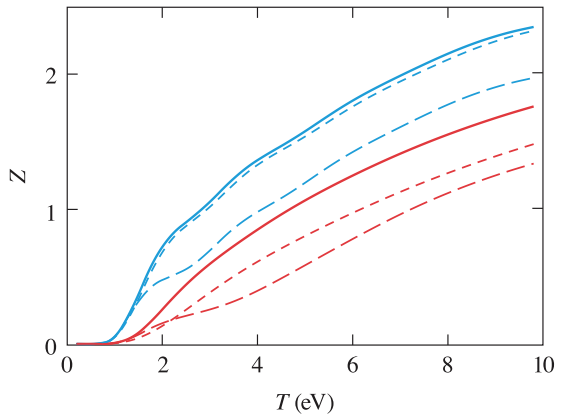

FIG. 2. Average ionization state Z as a function of temperature for mass densities 10^{-4} g/cm^3 (blue lines) and 10^{-2} g/cm^3 (red lines) with Debye-Hückel term omitted (short-dashed lines), Fermi term omitted (long-dashed lines), and with both terms retained in Eq. (1) (solid lines).

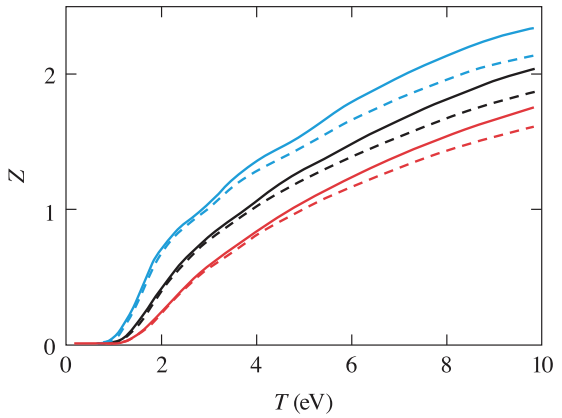

FIG. 3. Average ionization state Z as a function of temperature for mass densities 10^{-4} g/cm^3 (blue lines), 10^{-3} g/cm^3 (black lines), and 10^{-2} g/cm^3 (red lines) for 50%C-50%H (solid lines) and 42.5%C-57.5%H (dashed lines).

thermal effects depend on density and temperature and may be taken into account by using the XC GGA functional with explicit temperature dependence [45]. At lower temperatures (1 eV), the DFT method produces higher Z than SFDH. It is caused by the self-interaction error inherent in the DFT local and semilocal approximations for the XC energy [46]. The electron self-interaction decreases the ionization energy of H and to a lesser degree C atoms and leads to artificial increase in Z, which is more apparent for temperatures much smaller than ionization energies. The ionization states from AOT (black dashed lines) and CRE (blue dotted lines) tables are both within 0.2 from Z obtained with the DFT.

Figure 2 illustrates the relative importance of the Fermi short-range interaction term F_b and Debye-Hückel Coulomb interaction term F_c for the ionization state Z under considered conditions. At higher density $\rho = 10^{-2}$ g/cm^3 Fermi and Debye-Hückel terms are both essential to calculate Z (see red lines in Fig. 2). At lower density $\rho = 10^{-4}$ g/cm^3 only the Fermi term is essential, while the Debye-Hückel term contribution is negligible (see blue lines in Fig. 2). The Fermi term determines the cutoff in the partition function sum, see Eq. (11), while the Debye-Hückel term becomes unimportant at high temperatures and at low densities when $kT \gg \Delta I_{mi} \sim \sqrt{\rho/T}$, see Eq. (13).

In ICF experiments CH material can have a range of different atomic ratios of C and H. Figure 3 compares the dependence or ionization state Z on temperature for two common atomic ratios of C and H (50 %C-50 %H for polystyrene and 42.5 %C-57.5 %H for glow discharge polymer) calculated with the SFDH method. The difference is within 5% for the considered densities and temperatures. This is important because *ab initio* simulations for arbitrary atomic ratios in the material composition require large number of atoms in the simulation box to exactly match the atomic ratios in the material composition and are prohibitively computationally expensive. Using SFDH method, we found the following simple mixing rule that allows one to easily obtain Z for an arbitrary atomic ratio of C in CH, r, that is between two atomic ratios r_1 and r_2 for which SFDH-calculated Z is Z_1 and Z_2 respectively:

$$Z = \frac{r_2 - r}{r_2 - r_1} Z_1 + \frac{r - r_1}{r_2 - r_1} Z_2.$$

The value of Z found using this formula for any r between $r_1 = 42.5\%$ and $r_2 = 50\%$ considered above is within 0.1% of SFDH-calculated Z.

IV. DIELECTRIC CONSTANT OF H AND C AT ZERO TEMPERATURE

In this section, to assess the accuracy of the DFT method in calculating optical properties of H and C, we compare the dynamic polarizability of H atom in ground state calculated exactly from quantum mechanics to that from the DFT calculations. For a C atom, we compared the static atomic polarizability calculated with the DFT to the currently recommended value from the literature.

The DFT polarizabilities of H and C were calculated using the Kubo–Greenwood formulation [34] implemented in the KGEC@QUANTUM-ESPRESSO package. Calculations were performed using the SCAN meta-GGA XC functional and a single atom placed in the cubic simulation cell. The size of the simulation cell was large enough to ensure that the obtained polarizabilities do not depend on the size of the box and represent the polarizability of an isolated atom.

To compare with DFT, we calculated exactly the dynamic polarizability α of hydrogen atom in an external electric field of frequency ω using the following quantum mechanics formula [47]

$$\alpha = \frac{e_0^2}{m_e} \sum_k \frac{f_{kl}}{\omega_{kl}^2 - \omega^2}, \tag{18}$$

where $\omega_{kl} = (E_k - E_l)/\hbar$ and $E_{k(l)}$ is the energy of the atomic state $k(l)$, the oscillator strength of $l \to k$ transition f_{kl} is given by

$$f_{kl} = \frac{2m_e\omega_{kl}}{\hbar} |x_{kl}|^2, \tag{19}$$

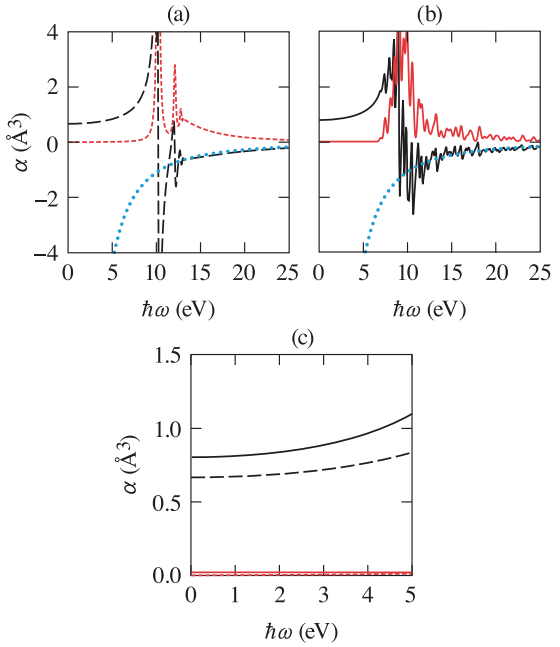

FIG. 4. (a) The real (black dashed line) and imaginary (red dashed line) parts of polarizability of H from exact theory and the high-frequency limit of polarizability $\alpha_{\rm hf}$ (blue dotted line). (b) The real (black solid line) and imaginary (red solid line) parts of polarizability of H from DFT calculations and the high-frequency limit of polarizability $\alpha_{\rm hf}$ (blue dotted line). (c) Zoomed-in part of (a) and (b) showing polarizabilities in the photon energy range of 0 to 5 eV from the exact theory and DFT calculations.

and x_{kl} are dipole matrix elements of the hydrogen atom. The oscillator strengths satisfy Thomas-Reich-Kuhn sum rule $\sum_k f_{kl} = 1$ [47], which was verified in our calculations.

Figure 4 shows the real and imaginary parts and high-frequency limit, $\alpha_{\rm hf} = -e_0^2/(m_e\omega^2)$, of hydrogen polarizability α in an external electric field with frequency ω as a function of ω. Figure 4(a) shows results of exact calculations using Eqs. (18) and (19) and the hydrogen energy eigenfunctions of discrete and continuous spectrum [48,49], and Fig. 4(b) shows the results of our DFT calculations. Static polarizability (at $\omega = 0$) of hydrogen from the exact calculations is 0.667 Å^3 (a well-known result, see, e.g., Ref. [48]) which is 15% lower than 0.78 Å^3 from the DFT calculations. Here and below we present polarizabilities in CGS units. At the optical probe frequency $\omega_0 = 2\pi c/\lambda_0$ (where c is the speed of light), $\hbar\omega_0 = 4.71$ eV, the polarizability of hydrogen from the exact calculations is 0.82 Å^3 which is 20% lower than 1.03 Å^3 from the DFT calculations.

Since atom of carbon is a multielectron system, its polarizability cannot be calculated exactly as for hydrogen and must be computed numerically or measured experimentally. Atomic polarizabilities for many elements from multiple sources are compiled in the latest *CRC Handbook of Physics and Chemistry* [35]. For carbon atom only simulated values are available and are based on comparison of results from eight modern computational methods (see Ref. [36]). The currently recommended in Ref. [35] value for the static polarizability of carbon is 1.67 Å$^3 \pm 2\%$. It is 6% higher than 1.58 Å^3 from our DFT calculations. There is no available reference data at the optical probe frequency for atomic polarizability of carbon, which is 2.62 Å^3 in our DFT calculations.

Self-interaction error inherent in the Kohn-Sham DFT local and semilocal approximations for the XC energy effectively increases the bound state energies and decreases the excited state energies relative to the ground state [46], thereby producing higher atomic polarizability. However, the effect is significantly reduced in the case of C with multiple electrons and the DFT-calculated polarizability is much closer to the reference data.

Having found atomic polarizabilities of C and H atoms, one can obtain the dielectric constant ϵ_b of a low-density CH gas at zero temperature using the following formula [47]

$$\epsilon_b = 1 + 4\pi[r\alpha_C + (1-r)\alpha_H]n_i, \tag{20}$$

where n_i is the number of C and H ions per unit volume in Å^{-3} and r is (as before) the atomic ratio of carbon atoms. Using DFT-calculated atomic polarizabilities at the optical probe frequency, $\alpha_H = 1.03$ Å^3 and $\alpha_C = 2.62$ Å^3, we find for 50 %C-50 %H ($r = 0.5$):

$$\epsilon_b = 1 + 4\pi\, 1.8\,\text{Å}^3 n_i, \tag{21}$$

From Eq. (20) one can see that the relative error of a method in calculating $(\epsilon - 1)$ is the same as that in calculating atomic polarizabilities. So we could estimate the error bound of the DFT method in calculating $(\epsilon - 1)$ to be about 20%—the largest of the errors of the DFT method in calculating polarizabilities of C and H found above.

V. DIELECTRIC CONSTANT OF CH AT TEMPERATURES OF FEW ELECTRON VOLTS

In this section, we obtain the dielectric constant of a few-electronvolt temperature partially ionized CH gas using the DFT and Kubo-Greenwood formulation. As in the previous section, the calculations were performed with the KGEC@QUANTUM-ESPRESSO package and the simplified scheme with two atoms placed in the fixed bcc positions. We expect that the use of advanced SCAN meta-GGA XC improves the accuracy of optical property predictions compared to PBE XC. In these calculations we employed the *all-electron* local pseudopotentials [50,51], required for the SCAN XC implementation in the KGEC@QUANTUM-ESPRESSO computational package, with the plane-wave energy cutoff of 4.8 keV. A downside of using *all-electron* pseudopotentials with such a high energy cutoff is that it makes calculations of optical properties for densities below 10^{-3} g/cm^3 or temperatures above 5 eV computationally unfeasible.

Figure 5 shows the dielectric constant of CH (at the laser probe wavelength of 263 nm) for 10^{-2} and 10^{-3} g/cm^3 densities from the DFT calculations at 1-, 3-, and 5-eV temperatures (red circles). For comparison, blue solid lines in Fig. 5 show the dielectric constant of a free-electron gas,

$$\epsilon_p = 1 - 4\pi 4.9\ \text{Å}^3 n_e, \tag{22}$$

where n_e is the density of free electrons in Å^{-3},

$$n_e = Zn_i, \tag{23}$$

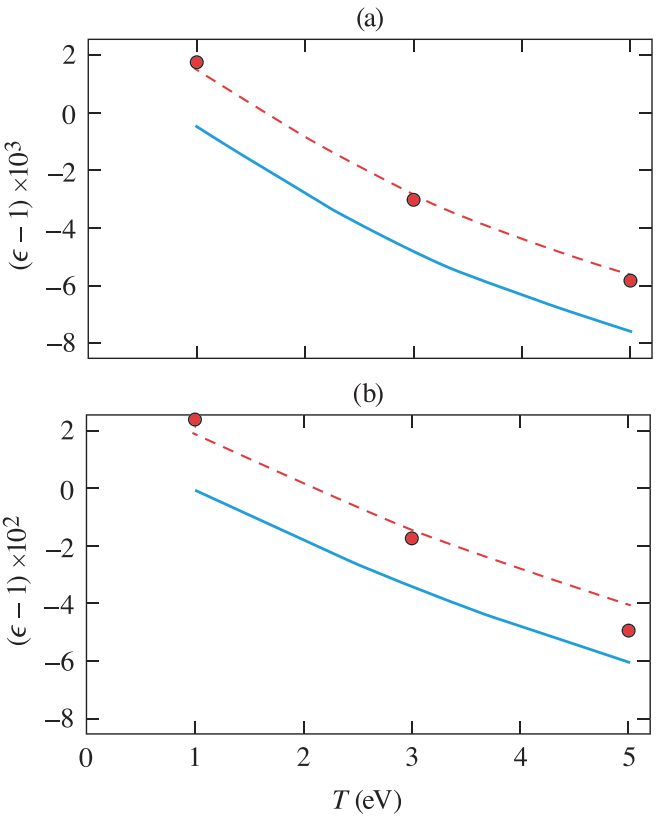

FIG. 5. The real part of the dielectric permittivity in CH as a function of temperature from DFT calculations (red circles), from Eq. (25) (red dashed lines), and from Eq. (22) (blue solid lines) for mass densities of (a) 10^{-3} g/cm^3 and (b) 10^{-2} g/cm^3.

n_i is the ion density in Å^{-3},

$$n_i = \frac{\rho}{\langle A\rangle}, \tag{24}$$

and $\langle A\rangle = 6.5$ amu is the average ion mass for 50 %C-50 %H. Equation (22) is the usual dielectric constant of plasma $\epsilon_p = 1 - n_e/n_c$ [52], where the critical plasma density $n_c = \epsilon_0 m_e\omega_0^2/e_0^2 = 1/(4\pi 4.9)$ Å^{-3}. As expected for a free-electron gas the dielectric constant Eq. (22) is smaller than 1, and it depends on the temperature through Z [see Eq. (23], which increases with temperature (as in Fig. 1) and makes $(\epsilon_p - 1)$ more negative (see Fig. 5).

We fitted the dielectric constant from DFT calculations (red dashed lines in Fig. 5) adding a positive term proportional to the number of ions to the plasma dielectric constant [Eq. (22)] as follows:

$$\epsilon_{\rm DFT} = 1 + 4\pi(1.7\ \text{Å}^3 n_i - 4.9\ \text{Å}^3 n_e). \tag{25}$$

The positive term is Eq. (25) describes the contribution from atomic polarizabilities (i.e., contributions from bound states of electrons in atoms). At low temperatures ($T \lesssim 1$ eV) a CH gas consists mostly of neutral (albeit excited) atoms and its dielectric constant approaches that of the zero-temperature CH gas considered in the previous section [compare Eq. (25) with $n_e = 0$ to Eq. (21)]. As the temperature increases, the ionization state Z and the number of free electrons increase making the dielectric constant smaller (and eventually less than one as in a plasma). Figure 5 shows that the approximate formula [Eq. (25)] fits well the DFT results especially at lower density of 10^{-3} g/cm^3 more relevant to the shock-release experiment considered in the next section.

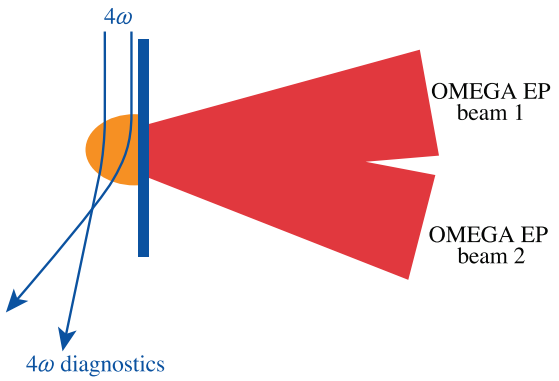

FIG. 6. The experimental setup used two OMEGA EP beams to drive a CH foil. The 4ω laser interferometry was used to measure the low-density profile in the rarefaction wave.

VI. SHOCK-RELEASE EXPERIMENTS

In this section we evaluate the impact of using a DFT-calculated dielectric constant on the electron density obtained from the interferometry measurement in the shock release experiments [6]. The experimental setup (Fig. 6) used two OMEGA EP laser beams that illuminated the 37-μm-thick CH foil with a 5-ns square pulse at 3×10^{14} W/cm^2 intensity. The electron density profiles were obtained from interferometry images at 1, 2, 3, and 4 ns into the laser drive using the 263-nm UV laser interferometry as briefly described below.

Interferometry images are formed by interference between the laser beam propagating through the plasma region of interest and the reference laser beam propagating through the vacuum. The interference pattern is determined by the spatial profile of the plasma index of refraction $n(\vec{x})$. Under certain simplifying assumptions (e.g., cylindrical symmetry as in [6]) one can reconstruct spatial profiles of the index of refraction from the interferometry images. In Ref. [6] the standard plasma index of refraction $n_p = \sqrt{\epsilon_p}$, which depends only on the electron density, was used in equation $n_p = n(\vec{x})$ to obtain the electron density $n_{e(p)}(\vec{x}) = n_c[1 - n(\vec{x})^2]$.

In general, the index of refraction depends on two variables, mass density and temperature, thereby precluding a unique restoration of the electron density from the index of refraction. In the low-density region of the shock-release CH material, which is accessible by the 4ω probe interferometry [6], the temperature is nearly constant and is about 5 eV consistent with radiation-hydrodynamics simulations [53], making the index of refraction a function of one variable and enabling unique restoration of the electron density.

Here we use more accurate DFT-calculated index of refraction $n_{\rm DFT} = \sqrt{\epsilon_{\rm DFT}}$ [where $\epsilon_{\rm DFT}$ is given by Eq. (25)] in equation $n_{\rm DFT} = n(\vec{x})$ to deduce the electron density $n_{e({\rm DFT})}(\vec{x})$. Since the same index of refraction profile $n(\vec{x})$ is used to obtain both $n_{e(p)}(\vec{x})$ and $n_{e({\rm DFT})}(\vec{x})$, the equation

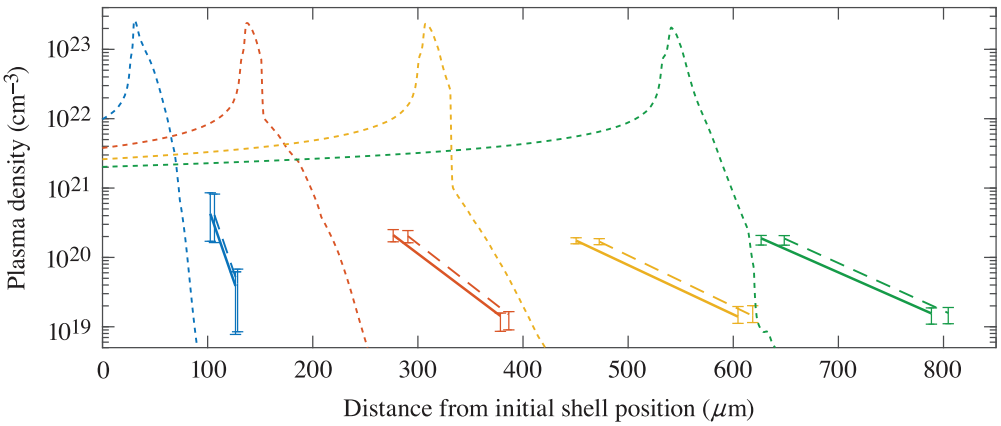

FIG. 7. Electron density profiles obtained from radiation-hydrodynamics simulations (short-dashed lines) and from experiments using plasma dielectric constant (22) (solid lines) and DFT-calculated dielectric constant (25) (long-dashed lines) at 1 ns (blue), 2 ns (red), 3 ns (yellow), and 4 ns (green).

connecting them is simply

$$n_p = n_{\mathrm{DFT}}, \tag{26}$$

which after substituting Eqs. (25) and (22) gives the equation for the ion density $n_i(\vec{x})$:

$$\begin{aligned} 1.7n_i(\vec{x}) - 4.9Z[n_i(\vec{x}) \cdot \langle A\rangle, T_0]n_i(\vec{x}) \\ = -4.9\, n_{e(p)}(\vec{x}), \end{aligned} \tag{27}$$

where $T_0 = 5$ eV. Having found $n_i(\vec{x})$, one obtains the electron density from

$$n_{e(\mathrm{DFT})}(\vec{x}) = Z[n_i(\vec{x}) \cdot \langle A\rangle, T_0]n_i(\vec{x}).$$

Figure 7 shows the electron density profiles $n_{e(p)}$ (solid lines) and $n_{e(\mathrm{DFT})}$ (long-dashed lines) as a function of a distance from the initial shell position along the center of the drive for four time moments. Short-dashed lines correspond to the electron densities from radiation-hydrodynamic simulations from Ref. [6]. To quantify the difference between the two electron density profiles (solid and long-dashed lines in Fig. 7), one can write Eq. (26) in the following form:

$$n_{e(\mathrm{DFT})} = \frac{n_{e(p)}}{1 - 1.7/(4.9Z)}. \tag{28}$$

The maximum relative difference between $n_{e(\mathrm{DFT})}$ and $n_{e(p)}$ is reached at smallest value of Z, which is $\sim$1.2 for experimental electron densities in Fig. 7. According to Eq. (28), the electron density $n_{e(\mathrm{DFT})}$ at a given position can be up to 40% higher than $n_{e(p)}$. Another interpretation is that the position of the rarefaction wave is farther away from the initial shell position by $\ln(1.4)L$, where L is the scale length of the electron density in the rarefaction wave. Since $L \sim 60$ μm at 4 ns, the rarefaction wave is at most 20 μm farther away from the shell, which is comparable to the experimental error bars.

The experimentally measurable electron density range is $(1.4 \times 10^{19}\mathrm{to}4.3 \times 10^{20})$ cm^{-3} and varies depending on the time of the measurement (see Fig. 7). It corresponds to the mass density range of $(6.3 \times 10^{-5}\mathrm{to}3.3 \times 10^{-3})$ g/cm^3 obtained from Eq. (24) using $n_i(\vec{x})$ from Eq. (27).

In the shock-release experiments that use lower laser-drive intensities, the temperatures and Z in the rarefaction wave are lower, and the plasma index of refraction differs more from the DFT-calculated index of refraction [see Eq. (28)] and cannot be used for extracting the electron densities from the interferometry data.

VII. CONCLUSIONS

In this article, we used a combination of semianalytical SFDH (based on the free energy minimization) and DFT *ab initio* approaches to calculate the ionization state Z and the dielectric constant in rarefied CH material at few electronvolt temperatures. The ionization state calculated with both SFDH and DFT methods was compared to that from two widely used ionization state tables (AOT and CRE). All four methods produced Z within 0.2 from each other. The SFDH equations and the algorithm for solving them can be readily used for any low-density multispecies plasmas.

The accuracy of the DFT method in calculating optical properties of cold rarefied CH was assessed by comparing the DFT-calculated atomic polarizabilities for H and C atoms to an analytical formula for H and the latest reference value for C from the *CRC Handbook of Physics and Chemistry*. The accuracy of DFT polarizabilities was estimated to be better than 20%. The DFT was used to calculate dielectric constant of CH for several temperature and density values and fitted with a simple analytical formula that contains an extra positive term due to contribution from atomic polarizabilities (i.e., contributions from bound states of electrons in atoms). This term is not present in the formula for the plasma dielectric constant.

The index of refraction calculated with the DFT method was used to revisit the interferometry data from Ref. [6]. Electron densities were found to be up to 40% higher and the position of the rarefaction wave up to 20 μm farther than reported in Ref. [6]. It is important to note that for a laser drive of lower intensities than in Ref. [6], the plasma index of refraction is not valid and a more-accurate DFT index of refraction must be used in the analysis of the shock-release experiments.

ACKNOWLEDGMENTS

We acknowledge useful conversations with I. V. Igumenshchev, A. A. Solodov, and D. H. Froula. The authors also thank S. Goedecker for creating and providing an accurate all-electron local pseudopotential for carbon used in this work.

This material is based on work supported by the Department of Energy National Nuclear Security Administration under Award No. DE-NA0003856, the University of Rochester, and the New York State Energy Research and Development Authority. This report was prepared as an account of work sponsored by an agency of the U.S. Government. Neither the U.S. Government nor any agency thereof, nor any of their employees, makes any warranty, express or implied, or assumes any legal liability or responsibility for the accuracy, completeness, or usefulness of any information, apparatus, product, or process disclosed, or represents that its use would not infringe privately owned rights. Reference herein to any specific commercial product, process, or service by trade name, trademark, manufacturer, or otherwise does not necessarily constitute or imply its endorsement, recommendation, or favoring by the U.S. Government or any agency thereof. The views and opinions of authors expressed herein do not necessarily state or reflect those of the U.S. Government or any agency thereof.

APPENDIX

In this Appendix, we outline a simple and robust method to numerically solve the system of Eqs. (9), (10), (13), (14), and (15) for the number of bound states of each ion of each species N_{mij} and the number of free electrons N_e in a unit volume. In addition to the total number of ions of each species (i.e., densities of species) N_m and the temperature T, the system contains as parameters for each bound state of each ion type of each species its excitation energy, degeneracy, and effective radius. The effective radius, r_{mij}, of species m of ion type i in bound state j with excitation energy $E^*_{mij} = E_{mij} - E_{mi0}$ is taken to be equal to the radius of the electron orbit in a classical hydrogen-like atom with charge Z_{mi} and energy E^*_{mij},

$$r_{mij} = \frac{a_0/Z_{mi}}{\left(1 - \frac{E^*_{mij}}{I_{mi}}\right)}, \tag{A1}$$

where $a_0 = 0.529$ Å is the Bohr radius and I_{mi} is the ionization energy of the ion. The excitation energies and degeneracies of bound states and the ionization energies for hydrogen H I and types of carbon ions C I,…,C VI were taken from NIST tables [38]. The system of Eqs. (9), (10), (13), (14), and (15) includes 932 ion densities N_{mij} plus the free-electron density N_e and is solved by iterations in the following way. We start iterations setting $N^0_{mij} = N_m\delta_{i0}\delta_{j0}$, $N^0_{mi} = N_m\delta_{i0}$, $N^0_e = 0$, where δ_{ij} is the Kronecker delta and the upper index denotes the iteration number. To start the nth iteration, we calculate u^n_{mi} using Eq. (11), then substitute u^n_{mi} into Eq. (9) and obtain N^n_{mij}, then substitute u^n_{mi} and N^n_{mij} into right-hand side of Eq. (13). At this point Eqs. (13), (14), and (15) constitute a system of 10 equations with respect to 10 unknowns: $N^n_{H0}, N^n_{H1}, N^n_{C0}, N^n_{C1}, \ldots, N^n_{C6}$, and N^n_e. Using Eq. (13) we express N^n_{mi} with $i > 0$ via N^n_{m0} and N^n_e, then using Eq. (14) we express N^n_{m0}, hence all N^n_{mi}, via N^n_e, After substituting them into Eq. (15) we obtain a polynomial equation of eighth order with respect to one unknown N^n_e. We find all eight roots of this polynomial using Mathematica [54]. Only one of the roots corresponds to the physical solution $N^n_e \geqslant 0$. Using it we obtain all N^n_{mi} and conclude the nth iteration. We repeat the iterations until

$$\sqrt{\sum_{mi}\left(N^n_{mi} - N^{n-1}_{mi}\right)^2} < \delta_{\rm acc}\sum_m N_m$$

for a desired value of accuracy $\delta_{\rm acc}$. After finding the number of ions N_{mi} and free electrons N_e, we use Eq. (17) to obtain the average ionization state Z. Using the outlined above procedure, we calculate Z for a range of desired CH densities and temperatures.

The method described in this Appendix is robust because the system of Saha Eqs. (13), (14), and (15) is transformed into a single polynomial equation, for which there are standard reliable algorithms (e.g., the Aberth method [55]) for finding all roots. This method can be applied to a system with any ion composition.

[1] J. Nuckolls, L. Wood, A. Thiessen, and G. Zimmerman, Nature (Lond.) **239**, 139 (1972).

[2] J. D. Lindl, Phys. Plasmas **2**, 3933 (1995).

[3] R. S. Craxton, K. S. Anderson, T. R. Boehly, V. N. Goncharov, D. R. Harding, J. P. Knauer, R. L. McCrory, P. W. McKenty, D. D. Meyerhofer, and J. F. Myatt *et al.*, Phys. Plasmas **22**, 110501 (2015).

[4] E. M. Campbell, V. N. Goncharov, T. C. Sangster, S. P. Regan, P. B. Radha, R. Betti, J. F. Myatt, D. H. Froula, M. J. Rosenberg, I. V. Igumenshchev *et al.*, Matter Radiat. Extremes **2**, 37 (2017).

[5] A. Howard, D. Haberberger, R. Boni, R. Brown, and D. H. Froula, Rev. Sci. Instrum. **89**, 10B107 (2018).

[6] D. Haberberger, A. Shvydky, V. N. Goncharov, D. Cao, J. Carroll-Nellenback, S. X. Hu, S. T. Ivancic, V. V. Karaseiv, J. P. Knauer, A. V. Maximov, and D. H. Froula, Phys. Rev. Lett. **123**, 235001 (2019).

[7] J. H. Kelly, L. J. Waxer, V. Bagnoud, I. A. Begishev, J. Bromage, B. E. Kruschwitz, T. J. Kessler, S. J. Loucks, D. N. Maywar, R. L. McCrory, D. D. Meyerhofer, S. F. B. Morse, J. B. Oliver, A. L. Rigatti, A. W. Schmid, C. Stoeckl, S. Dalton, L. Folnsbee, M. J. Guardalben, R. Jungquist, M. J. Shoup III, and D. Weiner *et al.*, J. Phys. IV France **133**, 75 (2006).

[8] M. Koenig, F. Philippe, A. Benuzzi-Mounaix, D. Batani, M. Tomasini, E. Henry, and T. Hall, Phys. Plasmas **10**, 3026 (2003).

[9] W. Theobald, J. E. Miller, T. R. Boehly, E. Vianello, D. D. Meyerhofer, T. C. Sangster, J. Eggert, and P. M. Celliers, Phys. Plasmas **13**, 122702 (2006).

[10] N. Ozaki, T. Sano, M. Ikoma, K. Shigemori, T. Kimura, K. Miyanishi, T. Vinci, F. H. Ree, H. Azechi, T. Endo *et al.*, Phys. Plasmas **16**, 062702 (2009).

[11] M. A. Barrios, D. G. Hicks, T. R. Boehly, D. E. Fratanduono, J. H. Eggert, P. M. Celliers, G. W. Collins, and D. D. Meyerhofer, Phys. Plasmas **17**, 056307 (2010).

[12] S. X. Hu, L. A. Collins, J. P. Colgan, V. N. Goncharov, and D. P. Kilcrease, Phys. Rev. B **96**, 144203 (2017)

[13] X. Zhang, G. Wang, B. Luo, F. Tan, S. N. Bland, J. Zhao, C. Sun, and C. Liu, J. Mater. Sci. **53**, 12628 (2018).

[14] D. V. Knyazev and P. R. Levashov, Comput. Mater. Sci **79**, 817 (2013).

[15] L. Caldern, V. V. Karasiev, and S.B. Trickey, Comput. Phys. Commun. **221**, 118 (2017).

[16] W. F. Huebner, A. L. Merts, N. H. Magee, Jr., and M. F. Argo, Los Alamos National Laboratory, Los Alamos, NM, Report LA-6760-M (1977).

[17] R. Epstein, T. J. B. Collins, J. A. Delettrez, S. Skupsky, and R. P. J. Town, Bull. Am. Phys. Soc. **43**, 1666 (1998).

[18] J. J. MacFarlane, I. E. Golovkin, and P. R. Woodruff, J. Quant. Spectrosc. Radiat. Transf. **99**, 381 (2006).

[19] H. K. Chung, M. H. Chen, W. L. Morgan, Y. Ralchenko, and R. W. Lee, High Energy Density Phys. **1**, 3 (2005).

[20] S. X. Hu, L. A. Collins, V. N. Goncharov, J. D. Kress, R. L. McCrory, and S. Skupsky, Phys. Plasmas **23**, 042704 (2016)

[21] J. Delettrez, R. Epstein, M. C. Richardson, P. A. Jaanimagi, and B. L. Henke, Phys. Rev. A **36**, 3926 (1987).

[22] P. B. Radha, V. N. Goncharov, T. J. B. Collins, J. A. Delettrez, Y. Elbaz, V. Yu. Glebov, R. L. Keck, D. E. Keller, J. P. Knauer, J. A. Marozas *et al.*, Phys. Plasmas **12**, 032702 (2005).

[23] M. M. Marinak, G. D. Kerbel, N. A. Gentile, O. Jones, D. Munro, S. Pollaine, T. R. Dittrich, and S. W. Haan, Phys. Plasmas **8**, 2275 (2001).

[24] I. V. Igumenshchev, V. N. Goncharov, F. J. Marshall, J. P. Knauer, E. M. Campbell, C. J. Forrest, D. H. Froula, V. Yu. Glebov, R. L. McCrory, S. P. Regan *et al.*, Phys. Plasmas **23**, 052702 (2016).

[25] D. G. Hummer and D. Mihalas, Astrophys. J. **331**, 794 (1988).

[26] Ya. B. Zel'dovich and Yu. P. Raizer, *Physics of Shock Waves and High-Temperature Hydrodynamic Phenomena* (Academic Press, New York, 1966).

[27] E. Fermi, Z. Phys. **26**, 54 (1924).

[28] R. H. Fowler, *Statistical Mechanics* (Cambridge University Press, Cambridge, UK, 1936).

[29] P. Debye and E. Hückel, Phys. Z. **24**, 185 (1923).

[30] N. D. Mermin, Phys. Rev. **137**, A1441 (1965).

[31] M. V. Stoitsov and I. Z. Petkov, Ann. Phys. **184**, 121 (1988).

[32] R. M. Dreizler, in *The Nuclear Equation of State*, edited by W. Greiner and H. Stöcker, *NATO Science Series B* (Plenum Press, New York, 1989), Vol. 216, Part A, p. 521.

[33] G. Kresse and J. Hafner, Phys. Rev. B **47**, 558 (1993); **49**, 14251 (1994); G. Kresse and J. Furthmüller, *ibid.* **54**, 11169 (1996).

[34] R. Kubo, J. Phys. Soc. Jpn. **12**, 570 (1957); D. A. Greenwood, Proc. Phys. Soc. Lond. **71**, 585 (1958).

[35] J. R. Rumble, editor, *CRC Handbook of Chemistry and Physics* (Internet Version 2020), 101th ed. (CRC Press/Taylor & Francis, Boca Raton, FL, 2020)

[36] C. Thierfelder, B. Assadollahzadeh, P. Schwerdtfeger, S. Schäfer, and R. Schäfer, Phys. Rev. A **78**, 052506 (2008).

[37] L. D. Landau and E. M. Lifshitz, *Statistical Physics* (Pergamon Press, Oxford, 1980).

[38] A. Kramida, Yu. Ralchenko, J. Reader, and NIST ASD Team, NIST Atomic Spectra Database (version 5.8), https://physics.nist.gov/asd.

[39] J. P. Perdew, K. Burke, and M. Ernzerhof, Phys. Rev. Lett. **77**, 3865 (1996); erratum **78**, 1396 (1997).

[40] A. Baldcreschi, Phys. Rev. B **7**, 5212 (1973)

[41] J. Sun, A. Ruzsinszky, and J. P. Perdew, Phys. Rev. Lett. **115**, 036402 (2015).

[42] P. Giannozzi, S. Baroni, B. Nicola, N. Calandra, R. Car, C. Cavazzoni, D. Ceresoli, G. L. Chiarotti, M. Cococcioni, I. Dabo *et al.*, J. Phys.: Condens. Matter **21**, 395502 (2009).

[43] A. Blanchet, M. Torrent, and J. Clérouin, Phys. Plasmas **27**, 122706 (2020)

[44] V. V. Karasiev and S. X. Hu, Phys. Rev. E **103**, 033202 (2021).

[45] V. V. Karasiev, J. W. Dufty, and S. B. Trickey, Phys Rev. Lett. **120**, 076401 (2018).

[46] J. P. Perdew and A. Zunger, Phys. Rev. B **23**, 5048 (1981).

[47] A. S. Davydov, *Quantum Mechanics*, 2nd ed. (Pergamon Press, Oxford, 1976).

[48] L. D. Landau and E. M. Lifshitz, *Quantum Mechanics—Non-relativistic Theory*, 3rd ed. (Pergamon Press, New York, 1977).

[49] H. A. Bethe and E. E. Salpeter, *Quantum Mechanics of One- and Two-Electron Atoms* (Academic Press, New York, 1957).

[50] C. Hartwigsen, S. Goedecker, and J. Hutter, Phys. Rev. B **58**, 3641 (1998).

[51] V. V. Karasiev, T. Sjostrom, and S. B. Trickey, Phys. Rev. B **86**, 115101 (2012).

[52] J. D. Jackson, *Classical Electrodynamics*, 3rd ed. (Wiley, New York, 1999).

[53] A. Shvydky, D. Haberberger, D. H. Froula, V. N. Goncharov, S. X. Hu, I. V. Igumenshchev, J. A. Marozas, A. V. Maximov, and P. B. Radha, Bull. Am. Phys. Soc. **63**, BAPS.2018.DPP.CO4.9 (2018).

[54] Mathematica, Version 12.1, Wolfram Research, Inc., Champaign, IL https://www.wolfram.com/.

[55] O. Aberth, Math. Comput. **27**, 339 (1973); D. A. Bini and G. Fiorentino, Num. Alg. **23**, 127 (2000); J. M. McNamee, *Numerical Methods for Roots of Polynomials—Part I*, 1st ed. (Elsevier, Amsterdam, 2007).